

Quantum Erasure Imaging: Complementary Modalities and Indefinite Causal Order

Sean D. Huver¹ and Sanjaya Lohani²

¹NVIDIA

²Southern Methodist University

(Dated: September 1, 2025)

Quantum Erasure Imaging (QEI) turns delayed-choice erasure into a practical imaging protocol. Entangled photon pairs encode two classical modalities, absorption $T(x, y)$ and phase $\phi(x, y)$, that are reconstructed from a single run of time-tagged coincidences by retrospective sorting on a remote ancilla. Measuring the ancilla in H/V yields T via which-path information; D/A yields interference visibility $\propto \frac{2\sqrt{T}}{T+1} \cos \phi$; and a rotated orthonormal analyzer continuously trades between them. We derive balanced two-port estimators whose denominators are analyzer independent (completeness / no signaling), together with Fisher information and Cramér–Rao bounds that establish an equivalence to time division under labeled randomization. The advantages of QEI are operational: single-run acquisition, perfect co-registration, and remote / delayed mode choice. Additionally, we show that by inserting a quantum switch module, the same acquisition yields co-registered maps of commutator contrast and a per-pixel causal witness, advancing imaging into the process-matrix regime. We validate the protocol with Monte-Carlo simulations and outline a compact photonic implementation.

Concept and Significance.—QEI casts Wheeler’s delayed choice into an imaging protocol: from a single acquisition of time-tagged coincidences, a remote measurement on an entangled ancilla retrospectively sorts the same raw events to reconstruct either absorption (T) or phase (ϕ) images and, by rotating the ancilla analyzer, to continuously tune the relative weight of which-path information and interference contrast. This does not circumvent complementarity: the analyzer angle sets predictability and visibility in accordance with the standard bound (saturating it near $T \simeq 1$). Beyond complementarity, we show how the addition of a quantum-switch module pushes imaging into the process-matrix regime: the same acquisition yields commutator-contrast $C(x,y)$ and causal-witness $W(x,y)$ maps, imaging where transformations do not commute and where causal order becomes indefinite. The complete protocol delivers single-run acquisition of multiple co-registered modalities with the object arm unchanged and basis choices that can be randomized or delayed within the same dataset.

Related Work and Explicit Distinctions.—(i) Quantum-eraser experiments (incl. delayed choice) established context-dependent interference [1, 2]. QEI repurposes this specifically for *image formation* with explicit T/ϕ estimators from one dataset. (ii) Ghost imaging retrieves spatial structure via correlations [3–5]; QEI places the object *inside* an interferometer of the imaging arm and uses the ancilla basis to decode modalities. (iii) Imaging with undetected photons employs induced coherence [6]; QEI instead uses conditional post-selection on an entangled partner to switch between absorption and phase reconstructions from the same run. (iv) Scarcelli–Zhou–Shih demonstrated a two-photon imaging quantum eraser and a random delayed-choice version [7, 8] to exhibit wave/particle behavior in an imaging geometry.

We expand this prior work via four avenues: (a) *co-registered dual-modality* (T, ϕ) reconstructions from a single acquisition of the same clicks; (b) a *continuous, orthonormal analyzer sweep* in *2D images* with a *two-port* normalized estimator whose denominator is analyzer-independent (completeness/no-signaling); (c) *closed-form estimators and FI/CRBs* together with a precise *FIM equivalence to time-division*, clarifying that QEI’s benefits are operational rather than per-photon informational; and (d) an extension to the work using an *indefinite causal order* (ICO) module—a photonic quantum-switch “Jones microscope”—that images commutator contrast and evaluates a per-pixel causal-witness map, pushing imaging into the process-matrix regime [10–15].

Theoretical Framework.—We prepare polarization-entangled pairs via type-II spontaneous parametric down-conversion (SPDC) [16]:

$$|\Psi_0\rangle = \frac{1}{\sqrt{2}}(|H\rangle_A |H\rangle_B + |V\rangle_A |V\rangle_B). \quad (1)$$

PBS1 maps $|H\rangle_A \rightarrow$ Arm 1 (sample), $|V\rangle_A \rightarrow$ Arm 2 (reference), creating path-polarization entanglement:

$$|\Psi_1\rangle = \frac{1}{\sqrt{2}}(|H\rangle_{Arm1A} |H\rangle_B + |V\rangle_{Arm2A} |V\rangle_B). \quad (2)$$

The sample imparts transmission $T(x, y)$ and phase $\phi(x, y)$ in Arm 1. A half-wave plate in Arm 2 rotates $|V\rangle \rightarrow |H\rangle$ so both paths share polarization at recombination:

$$|\Psi_2\rangle = \frac{1}{\sqrt{2}}(|H\rangle_{Arm1A} |H\rangle_B + |H\rangle_{Arm2A} |V\rangle_B). \quad (3)$$

BS2 (50/50) maps

$$|H\rangle_{Arm1A} \rightarrow \frac{1}{\sqrt{2}}(|D1\rangle_A + |D2\rangle_A), \quad (4)$$

$$|H\rangle_{Arm2A} \rightarrow \frac{1}{\sqrt{2}}(|D1\rangle_A - |D2\rangle_A), \quad (5)$$

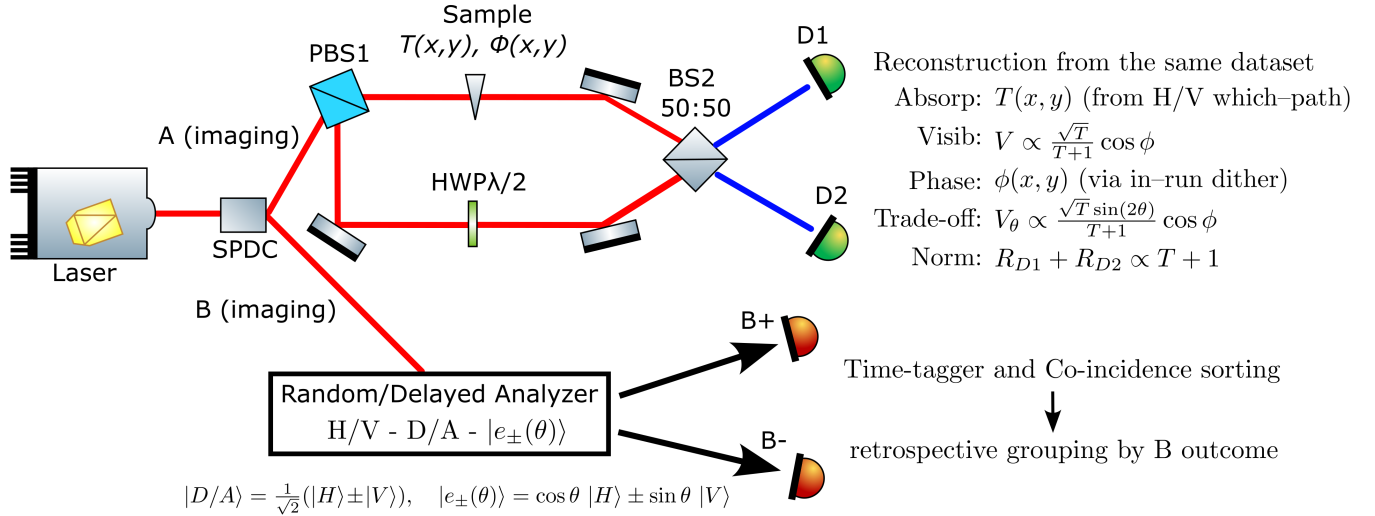


FIG. 1. **QEI schematic.** The imaging photon A traverses a modified Mach-Zehnder: PBS1 encodes which-path on polarization; the object in Arm 1 imparts $T(x, y), \phi(x, y)$; a HWP equalizes polarization; and BS2 recombines to two ports (D1,D2). The ancilla photon B is measured in a random/delayed analyzer (H/V, D/A, or a rotated orthonormal basis $\{|e_{\pm}(\theta)\rangle\}$). All events are time-tagged and retrospectively sorted by B 's outcome to reconstruct co-registered absorption and phase images from a single run. Two-port normalization makes the denominator analyzer-independent (completeness/no-signaling).

Capability	QEI (this work)	Imaging with Undetected Light (Lemos '14)	Single-Shot Phase/Visibility (Haase '23)	Entangled Holography (Defienne '21)	Entangled Pos-Mom Microscopy (2024)
Quantum resource	Entangled pairs (pol.)	Induced coherence	Induced coherence + pol.	Spatial/pol. ent. pairs	Pos-mom entangled pairs
Primary readout	Ancilla-sorted coinc.	Direct intensity	2-channel direct intensity	Correlations (hologram)	Near/far-field coinc.
Modality outputs	T & ϕ (same data)	T or phase (reconfig.)	Phase & Vis. ((~)for T)	Complex field (T & ϕ)	T & phase (via momentum)
Single-acquisition	✓	✗	✓(two channels)	✓(one dataset)	✓
Remote/delayed choice	✓(ancilla choice)	✗(toggle path)	✗(fixed encoding)	✗(fixed readout)	✗(fixed readout)
Continuous trade-off	✓(rotatable θ)	✗(binary)	✗(fixed mixing)	✗(fixed)	✗(fixed)
Two-port normalization	✓(θ -independent)	✗	✗	✗	✗
FI/CRB analysis	✓(T, ϕ)	✗	((~)(metrics))	((~)(fidelity))	((~)(precision))
Object arm unchanged	✓	✗(toggle)	✓	✓	✓
Perfect co-registration	✓(post-sorted)	✗(separate runs)	✓(simultaneous)	✓(same data)	✓(paired events)
2D scenes/samples	✓	✓	✓	✓	✓
ICO / causal-witness	✓(optional)	✗	✗	✗	✗
Operational advantage	Single-run, co-reg.	Undetected photons	Single-shot phase	Remote/incoherent phase	Background-resilient QPI

TABLE I. **Comparison of QEI with closely related quantum/entanglement-based imaging approaches.** Legend: ✓ = supported; ✗ = not supported; (~) = partial/conditional. “Dual modality” means recovering both absorption $T(x, y)$ and phase $\phi(x, y)$ (or equivalent contrast/phase) from a single acquisition. QEI uniquely combines: (i) single-run, co-registered T and ϕ via retrospective ancilla sorting; (ii) a *continuous* analyzer trade-off with two-port, analyzer-independent normalization; (iii) explicit FI/CRB analysis; and (iv) an optional indefinite-causal-order module for commutator-contrast and causal-witness imaging.

yielding

$$|\Psi_3\rangle = \frac{1}{2} \left[|D1\rangle_A (\sqrt{T} e^{i\phi} |H\rangle_B + |V\rangle_B) + |D2\rangle_A (\sqrt{T} e^{i\phi} |H\rangle_B - |V\rangle_B) \right]. \quad (6)$$

Reconstruction in canonical bases.—Measuring B in H/V has total which path information (WPI) of the pho-

ton, and we find at either port,

$$R(D1, H) \propto T, \quad R(D1, V) \propto 1 \quad (\text{and similarly for } D2), \quad (7)$$

so the two-port absorption estimator is

$$\hat{T}(x, y) = \frac{R(D1, H) + R(D2, H)}{R(D1, V) + R(D2, V)}. \quad (8)$$

To demonstrate the reconstruction process, we begin

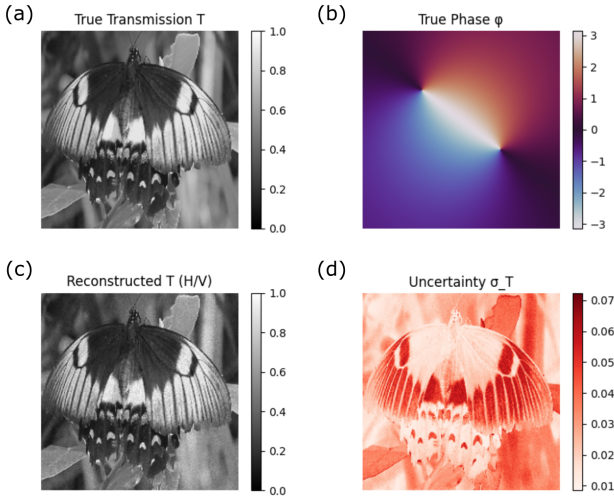


FIG. 2. Illustration of the reconstruction of $T(x, y)$ using H/V polarization bases. (a) Image representing True $T(x, y)$. (b) A vortex phase map associated with the sample. Measuring B : (c) Reconstructed $T(x, y)$. (d) Estimated uncertainty in the reconstructed $T(x, y)$.

with an image [18] representing the true transmission function $T(x, y)$, shown in Fig. 2 (a). After that, a vortex phase map, $\phi(x, y)$, is simulated and presented in Fig. 2 (b). A single acquisition with 1000 photons per pixel is then performed by measuring B in H/V bases. Using the coincidence counts recorded at detectors D1 and D2, the transmission function $T(x, y)$ is reconstructed. The resulting reconstruction and its associated uncertainty are shown in Fig. 2 (c) and Fig. 2 (d), respectively. Moreover, we can clearly find a significant overlap between the true and reconstructed $T(x, y)$, as indicated in the histogram plot, Fig. 3 (a). We also find the correlation coefficient $r = 0.990$ between the true and reconstructed $T(x, y)$ as shown in Fig. 3 (b).

Similarly, measuring B in D/A with $|D/A\rangle = (|H\rangle \pm$

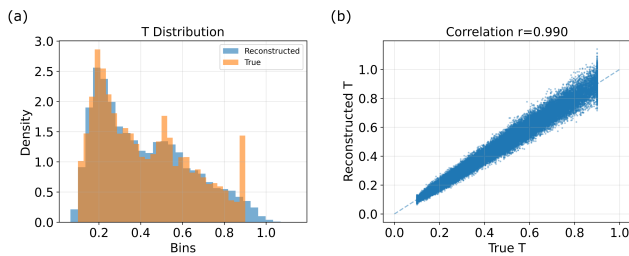


FIG. 3. Measuring B on H/V bases. (a) $T(x, y)$ Distribution: brown and blue histograms, respectively, represent the true $T(x, y)$ and reconstructed values of $T(x, y)$. (b) Correlation coefficient between the true T and reconstructed T at 1000 photons per pixel.

$|V\rangle)/\sqrt{2}$ yields, at D1,

$$R(D1, D) \propto T + 1 + 2\sqrt{T} \cos \phi, \quad (9)$$

$$R(D1, A) \propto T + 1 - 2\sqrt{T} \cos \phi, \quad (10)$$

and the opposite fringe at D2. The two-port normalized differential (equal to single-port visibility) is

$$\begin{aligned} V(x, y) &= \frac{[R(D1, D) - R(D1, A)] - [R(D2, D) - R(D2, A)]}{[R(D1, D) + R(D1, A)] + [R(D2, D) + R(D2, A)]} \\ &= \frac{2\sqrt{T(x, y)}}{T(x, y) + 1} \cos \phi(x, y). \end{aligned} \quad (11)$$

The visibility of a single acquisition for the example image is illustrated in Fig. 4. The resulting contrast of interference pattern while measuring B in D/A bases and its associated uncertainty are shown in Fig. 4 (a) and (b), respectively.

Intermediate analyzer: orthonormal rotation.—To continuously tune which-path vs. interference while remaining physical, we rotate B 's polarization in an *orthonormal* basis

$$|e_1(\theta)\rangle = \cos \theta |H\rangle + \sin \theta |V\rangle, \quad (12a)$$

$$|e_2(\theta)\rangle = -\sin \theta |H\rangle + \cos \theta |V\rangle. \quad (12b)$$

Projecting Eq. (6) onto $\{|e_{1,2}\rangle\}_B$, the D1 intensities are

$$R(D1, e_1) \propto T \cos^2 \theta + \sin^2 \theta + 2\sqrt{T} \sin \theta \cos \theta \cos \phi, \quad (13)$$

$$R(D1, e_2) \propto T \sin^2 \theta + \cos^2 \theta - 2\sqrt{T} \sin \theta \cos \theta \cos \phi, \quad (14)$$

with the interference term reversing sign at D2. Summing over $|e_{1,2}\rangle$ on a given port gives $T + 1$ (up to normalization), *independent of* θ , as required by completeness/no-signaling:

$$R(D1, e_1) + R(D1, e_2) \propto T + 1, \quad (15a)$$

$$R(D2, e_1) + R(D2, e_2) \propto T + 1. \quad (15b)$$

Using both ports, the normalized differential (generalizing Eq. (11)) is

$$V_\theta(x, y) = \frac{2\sqrt{T(x, y)} \sin(2\theta)}{T(x, y) + 1} \cos \phi(x, y), \quad (16)$$

which reduces to Eq. (11) at $\theta = \pi/4$ and vanishes at $\theta = 0, \pi/2$. Notably, for the two-port estimator the *denominator is θ -independent*.

Let N be the expected *coincidences per pixel* in one run; a fraction α is measured in H/V (WPI) and $\beta = 1 - \alpha$ in D/A or a rotated basis.

Absorption (T) from WPI.—Pooling both ports gives two outcomes $\{H, V\}$ with probabilities $p_H = T/(T + 1)$,

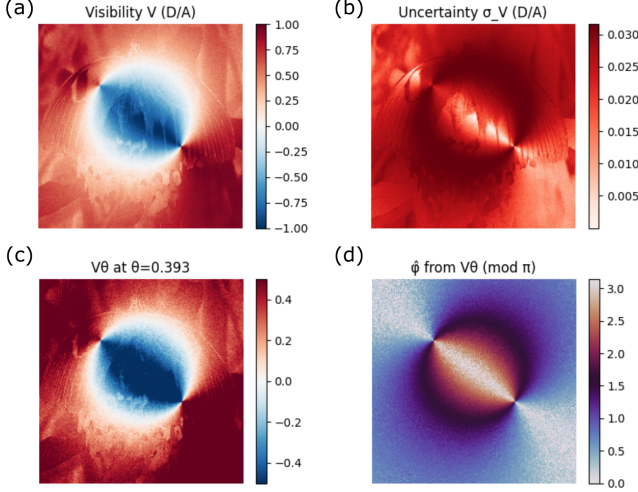


FIG. 4. Measuring B on D/A bases: (a) Two-port normalized differential corresponding to the given image $T(x, y)$. (b) Estimated uncertainty in the visibility derived from coincidence counting statistics. Measuring B on rotational $|e_{\pm}(\theta)\rangle$ bases: (c) Visibility evaluated at $\theta = \pi/8$. (d) Reconstruction of phase ϕ (modulo π) based on the visibility shown in panel (c).

$p_V = 1/(T + 1)$. With $S_T = \alpha N$ WPI-tagged coincidences,

$$\text{Var}[\hat{T}] \simeq \frac{T(1+T)^2}{S_T}, \quad \text{SNR}_T \simeq \frac{\sqrt{S_T T}}{1+T}. \quad (17)$$

This saturates the CRB for WPI-tagged events.

Phase (ϕ) from D/A .—Using both ports with $S_\phi = \beta N$ erasure-tagged coincidences, the per-event FI for ϕ is

$$\mathcal{I}_\phi^{(D/A)} = \frac{4T \sin^2 \phi}{(T+1)^2 - 4T \cos^2 \phi}, \quad (18)$$

and the CRB is $\text{Var}[\hat{\phi}] \geq 1/(\mathcal{I}_\phi^{(D/A)})$. At $T = 1$, $\mathcal{I}_\phi^{(D/A)} = 1$ for all ϕ .

Phase from the rotated basis.—For the orthonormal analyzer Eq. (12), the two-port per-event FI can be written compactly by defining

$$\begin{aligned} A &= T \cos^2 \theta + \sin^2 \theta, \\ B &= T \sin^2 \theta + \cos^2 \theta, \\ \Delta &= 2\sqrt{T} \sin \theta \cos \theta \cos \phi, \end{aligned}$$

as

$$\mathcal{I}_\phi^{(\theta)} = \frac{4T \sin^2 \theta \cos^2 \theta \sin^2 \phi}{T+1} \left[\frac{A}{A^2 - \Delta^2} + \frac{B}{B^2 - \Delta^2} \right], \quad (19)$$

which reduces at $T = 1$ to

$$\mathcal{I}_\phi^{(\theta)}|_{T=1} = \frac{\sin^2(2\theta) \sin^2 \phi}{1 - \sin^2(2\theta) \cos^2 \phi}, \quad (20)$$

maximized at $\theta = \pi/4$.

Single-port vs. two-port.—For D/A at any T , the per-used-event FI for a single port equals Eq. (18). Two-port processing therefore *doubles the information rate per detected pair* (it uses all coincidences) and yields a balanced normalized estimator [Eqs. (11), (16)]. Furthermore, the visibility of image acquisition on rotational $|e_{\pm}(\theta)\rangle$ bases at $\theta = \pi/8$ is shown in Fig. 4 (c).

Phase retrieval from $\cos \phi$.—Eqs. (11) and (16) provide $\cos \phi(x, y)$. To recover ϕ unambiguously one needs: (i) phase stepping (apply a known global dither δ on one interferometer arm during the same run and jointly fit $\cos \phi$ and $\cos(\phi + \delta)$), (ii) a brief second calibration run with a known phase offset, or (iii) spatial unwrapping with smoothness priors where valid. To illustrate phase retrieval, the estimated phase (mod π) using Eqs. (16) at $\theta = \pi/8$ is shown in Fig. 4 (d).

INFORMATION-THEORETIC ANALYSIS

For small parameter changes $\delta \boldsymbol{\vartheta}$ with $\boldsymbol{\vartheta} = (T, \phi)^\top$, local distinguishability is set by $D_{\text{KL}} \approx \frac{1}{2} \delta \boldsymbol{\vartheta}^\top \mathcal{J} \delta \boldsymbol{\vartheta}$, where the total FIM is

$$\mathcal{J} = S_T \mathcal{I}^{(\text{WPI})} + S_\phi \mathcal{I}^{(\text{erase/rot})}, \quad (21)$$

with $\mathcal{I}^{(\text{WPI})} = \text{diag}(\frac{1}{T(1+T)^2}, 0)$ and $\mathcal{I}^{(\text{erase/rot})}$ from Eqs. (18) or (19).

Equivalence to time-division.—**Proposition 1 (FIM equivalence under labeled randomization).** Consider QEI where each coincidence is recorded along with the ancilla basis/outcome, and the random choice over bases $\{\theta_k\}$ is independent of (T, ϕ) . Assume equal detection efficiencies across B outcomes and identical object-arm configuration, negligible drift and accidentals (or appropriately corrected). Then the *per-coincidence* FIM of QEI equals the convex combination of the per-coincidence FIMs of time-division experiments that run each basis θ_k for fraction w_k :

$$\mathcal{J}_{\text{QEI}} = \sum_k w_k \mathcal{J}(\theta_k).$$

Sketch. The observed outcomes include the label $(\theta_k, \text{outcome})$, so the log-likelihood decomposes as $\sum_i \log p(y_i | \theta_{k_i}; \boldsymbol{\vartheta})$. Taking expectations under the product measure with fixed $\{w_k\}$ gives $\mathbb{E}[-\partial_{\boldsymbol{\vartheta}}^2 \log \mathcal{L}] = \sum_k w_k \mathbb{E}[-\partial_{\boldsymbol{\vartheta}}^2 \log p(\cdot | \theta_k)]$, yielding the stated equality. \square

Operational advantage. By *operational* we mean advantages to *workflow and systematics*, not per-photon information: (i) *single-run* acquisition of both modalities without touching the object arm; (ii) *perfect co-registration* since both reconstructions derive from the same raw hits; (iii) *remote/delayed* basis choice (and continuous tuning) via the ancilla measurement, reducing drift/alignment risk relative to time-division.

IMAGING INDEFINITE CAUSAL ORDER: QUANTUM-SWITCH JONES MICROSCOPY

Motivation

Indefinite causal order (ICO) occurs when two operations act in a coherent superposition of alternative orders, a resource formalized by the process-matrix framework [10] and operationalized by the *quantum switch* [11]. ICO has been verified in photonic switches via *causal witnesses* that certify *causal nonseparability* (CNS) [13–15]. However, ICO has not yet been used to *form images* of a material property. Here we show how to upgrade our apparatus into a *quantum-switch Jones microscope* that produces, from a single acquisition, pixel-resolved maps of (i) commutator contrast—“where order matters”—and (ii) a causal-witness value, both co-registered with the usual $T(x, y)$ and $\phi(x, y)$. This pushes imaging into the process-matrix regime, beyond correlation-based quantum imaging.

ICO imaging could provide a novel contrast mechanism for characterizing complex anisotropic materials—such as metamaterials, liquid crystals, or stressed polymers—where the spatial arrangement and alignment of different optical properties (e.g., birefringence and dichroism) dictate the material’s function. ICO imaging offers a direct way to visualize the interplay and ordering of these interactions.

Protocol concept

At each pixel (x, y) the sample implements two polarization transformations that, in general, do not commute. We model them as Jones (possibly nonunitary) operators $U(x, y)$ and $V(x, y)$ acting on the imaging photon A. We embed these in a *quantum switch* so that the photon traverses the sequence

$$U \circ V \quad \text{and} \quad V \circ U$$

in a coherent superposition controlled by a qubit C. In practice, a Sagnac interferometer implements the control: the clockwise path applies U then V , the counter-clockwise path applies V then U ; the C-qubit is the path in the Sagnac and is measured at the output beam splitter in the $\{|+\rangle, |-\rangle\}$ basis [12, 14]. (Our two-port detection on A naturally realizes this $\{+, -\}$ readout.)

State picture. For an input polarization state $|\psi_{\text{in}}\rangle$, the joint evolution (up to a normalization set by losses) is

$$|\Psi_{\text{out}}\rangle \propto (UV \otimes |0\rangle_C + VU \otimes |1\rangle_C) |\psi_{\text{in}}\rangle, \quad (22)$$

so that postselecting C in $|+\rangle = (|0\rangle + |1\rangle)/\sqrt{2}$ or $|-\rangle = (|0\rangle - |1\rangle)/\sqrt{2}$ implements the *anti-commutator*

and *commutator* channels, respectively:

$$|\psi_+\rangle \propto (UV + VU) |\psi_{\text{in}}\rangle, \quad (23a)$$

$$|\psi_-\rangle \propto (UV - VU) |\psi_{\text{in}}\rangle. \quad (23b)$$

The corresponding intensities at pixel (x, y) obey

$$I_{\pm}(x, y) \propto \| (UV \pm VU) |\psi_{\text{in}}\rangle \|^2, \quad (24a)$$

$$I_+ + I_- \propto \|UV |\psi_{\text{in}}\rangle\|^2 + \|VU |\psi_{\text{in}}\rangle\|^2. \quad (24b)$$

Equation (24) immediately implies a *completeness/no-signaling* property: $I_+ + I_-$ is independent of the $\{+, -\}$ measurement basis of C (analogous to our Eq. (15) for the eraser analyzer). This makes two-port normalization particularly robust here as well.

Primary observable: commutator-contrast image

Define the *commutator-contrast* at each pixel,

$$C(x, y) = \frac{I_-(x, y)}{I_+(x, y) + I_-(x, y)} \in [0, 1], \quad (25)$$

which vanishes iff $[U(x, y), V(x, y)] = 0$ for the probed input polarization(s).

Operationally, we measure the coincidence rates $R(D_j, \pm)$ between the detectors $D_j \in \{D_1, D_2\}$ and the ancilla outcomes \pm . From these, we define the difference signal for each detector:

$$\Delta R_j = R(D_j, +) - R(D_j, -). \quad (26)$$

To account for imperfect experimental visibility, which we characterize by a factor $0 < \nu(x, y) \leq 1$, the balanced estimator for the commutator-contrast is constructed as

$$\hat{C}(x, y) = \frac{1}{\nu(x, y)} \frac{(\Delta R_1 - \Delta R_2)_{+\leftrightarrow-}}{\sum_{j=1}^2 (R(D_j, +) + R(D_j, -))}, \quad (27)$$

where the denominator is the total coincidence rate.[19]

Application: Mapping Material Structure and Stress (Jones optics). Let $U = R(\alpha, \Delta)$ be a linear retarder (representing birefringence) and $V = D(t_H, t_V)$ be a partial polarizer (representing dichroism). These transformations generally commute only if their principal axes are aligned. The $C(x, y)$ map directly visualizes this local alignment: Where the local optic axes render $[U, V] \neq 0$, $C(x, y)$ lights up; where they align (or $t_H = t_V$), $C(x, y) \approx 0$.

This has significant practical implications. For instance, in material science, $C(x, y)$ can be used to analyze internal stress and strain distributions. Stress often induces birefringence (U) which may not align with the material’s intrinsic structure or absorption properties (V). The commutator contrast provides a direct, spatially resolved map of these misaligned tensors. Furthermore, in the fabrication of layered optical metamaterials,

$C(x, y)$ can directly quantify the misalignment between successive layers, isolating fabrication errors that might be difficult to disentangle with conventional polarization microscopy.

Foundational observable: a per-pixel causal-witness map

Beyond $C(x, y)$, we construct a *causal witness* $\mathcal{W}(x, y)$ whose positive value certifies that the local process is not compatible with any definite (or probabilistic) order [15]. Practically, one fixes a small set of analyzer settings on the target (polarization projectors at the output of UV/VU), and uses the labeled outcomes $\{\mathbf{C} = \pm\}$ to evaluate a linear functional

$$\mathcal{W}(x, y) = \sum_{o, \pm} w_{o, \pm} P(o, \pm | x, y), \quad (28)$$

with coefficients $w_{o, \pm}$ chosen (from the witness-construction recipes in [15]) so that $\mathcal{W} \leq 0$ for all causally-separable processes but $\mathcal{W} > 0$ for the switch. We display $\mathcal{W}(x, y)$ as a heat map co-registered with $C(x, y)$, $T(x, y)$, and $\phi(x, y)$. *Remark.* If desired, a stronger, device-independent flavor is reachable by adding a spacelike-separated observer entangled to the control and testing the inequalities of Ref. [17] (beyond the scope of the present implementation).

Integration with our QEI workflow

- **Acquisition.** As in the main protocol, we record time-tagged coincidences with labels indicating the analyzer choice and outcome(s). For ICO, we label the $\mathbf{C} = \pm$ outcomes (read out by the Sagnac output ports or an equivalent path/polarization control). This is a purely *software-side* extension of our logging.
- **Normalization and stability.** Two-port processing carries over verbatim: the $\{+, -\}$ sum is analyzer-independent (completeness), yielding denominators like those in Eqs. (11), (16) that suppress gain drifts.
- **Information accounting.** With N total coincidences per pixel and a fraction γ devoted to ICO settings, the total Fisher information adds as in Eq. (21): $J_{\text{total}} = S_T I_{\text{WP}} + S_\phi I_{\text{erase/rot}} + S_{\text{ICO}} I_{\text{ICO}}$, with $S_{\text{ICO}} = \gamma N$ and I_{ICO} obtained from the binomial statistics of $\{\mathbf{C} = \pm\}$ and the chosen witness readouts.

Hardware minimality

A compact realization uses a polarization Sagnac: clockwise applies $U \circ V$, counter-clockwise $V \circ U$; the final beam splitter measures \mathbf{C} in $\{|+\rangle, |-\rangle\}$ [12, 14]. We then reuse exactly the same A-side two ports $D_{1,2}$ and the same detector technology (e.g., SPAD arrays [9]) as in our main QEI figures. No changes to the object arm are needed apart from inserting the two elements U, V (which can be existing Jones elements within the sample or an add-on birefringent/dichroic pair).

Claims enabled by this module

1. A **commutator-contrast image** $C(x, y)$ that vanishes where $[U, V] = 0$ and is nonzero where order matters.
2. A **causal-witness image** $\mathcal{W}(x, y)$ with $\mathcal{W} > 0$ in regions exhibiting CNS, evaluated from the same, single-run, time-tagged dataset.
3. A clear foundational distinction from classical mixtures: no randomized definite-order model generates the $|-\rangle$ interference term in Eq. (23) or produces $\mathcal{W} > 0$ [13–15].

Discussion

Standard quantum imaging leverages correlations to recover T or ϕ . The ICO module images a *different object property*: the algebraic non-commutativity of two local transformations and, via $\mathcal{W}(x, y)$, the causal structure of the induced process. To our knowledge, this constitutes the first proposal to produce *per-pixel causal-witness maps* and *commutator-contrast images* co-registered with conventional modalities, realized within a single acquisition using the same two-port normalization and labeling machinery that underpins our QEI estimators.

Discussion.—QEI provides both a *pedagogical window* and a *practical protocol*. Conceptually, the orthonormal analyzer sweep [Eqs. (12)–(16)] turns the abstract complementarity trade-off into a pixel-resolved morphing of images while respecting completeness/no-signaling [Eq. (15)]. Technically, the explicit estimators and FI/CRBs quantify performance and clarify that QEI’s advantages are operational: one run, co-registration, and a remote, even delayed, modality choice.

Conclusion.—We presented a theory of QEI with: (i) an *orthonormal* intermediate analyzer enabling a continuous trade-off, (ii) closed-form dual-modality estimators and visibilities [Eqs. (8), (11), (16)], (iii) singles/no-signaling checks, and (iv) FI/CRBs [Eqs. (18)–(20)] and a precise statement of information-theoretic equivalence

to time-division. These results sharpen QEI as both a clean visualization of complementarity and a convenient imaging protocol.

-
- [1] M. O. Scully and K. Driehl, Quantum eraser, *Phys. Rev. A* **25**, 2208 (1982).
- [2] Y.-H. Kim, R. Yu, S. P. Kulik, Y. Shih, and M. O. Scully, A delayed choice quantum eraser, *Phys. Rev. Lett.* **84**, 1 (2000).
- [3] T. B. Pittman, Y. H. Shih, D. V. Strekalov, and A. V. Sergienko, Optical imaging by means of two-photon quantum entanglement, *Phys. Rev. A* **52**, R3429 (1995).
- [4] R. S. Bennink, S. J. Bentley, and R. W. Boyd, “Two-Photon” coincidence imaging with a classical source, *Phys. Rev. Lett.* **89**, 113601 (2002).
- [5] I. A. Erkmen and J. H. Shapiro, Ghost imaging: from quantum to classical illumination, *Adv. Opt. Photon.* **2**, 405–450 (2010).
- [6] G. B. Lemos, V. Borish, G. D. Cole, S. Ramelow, R. Lapkiewicz, and A. Zeilinger, Quantum imaging with undetected photons, *Nature* **512**, 409–412 (2014).
- [7] G. Scarcelli, Y. Zhou, and Y. Shih, Random delayed-choice quantum eraser via two-photon imaging, *Phys. Rev. Lett.* **98**, 223601 (2007).
- [8] G. Scarcelli, Y. Zhou, and Y. Shih, Two-photon quantum eraser in imaging, *Phys. Rev. A* **72**, 051801(R) (2005).
- [9] C. Bruschini, H. Homulle, I. M. Antolovic, S. Burri, and E. Charbon, Single-photon avalanche diode arrays for quantum imaging, *Light: Science & Applications* **10**, 1 (2021).
- [10] O. Oreshkov, F. Costa, and Č. Brukner, Quantum correlations with no causal order, *Nature Communications* **3**, 1092 (2012).
- [11] G. Chiribella, G. M. D’Ariano, P. Perinotti, and B. Valiron, Quantum computations without definite causal structure, *Physical Review A* **88**, 022318 (2013).
- [12] L. M. Procopio, A. Moqanaki, M. Araújo, F. Costa, I. A. Calafell, E. G. Dowd, D. R. Hamel, L. A. Rozema, Č. Brukner, and P. Walther, Experimental superposition of orders of quantum gates, *Nature Communications* **6**, 7913 (2015).
- [13] G. Rubino, L. A. Rozema, A. Feix, M. Araújo, J. M. Zeuner, L. M. Procopio, Č. Brukner, and P. Walther, Experimental verification of an indefinite causal order, *Science Advances* **3**, e1602589 (2017).
- [14] K. Goswami, C. Giarmatzi, M. Kewming, F. Costa, C. Branciard, J. Romero, and A. G. White, Indefinite causal order in a quantum switch, *Physical Review Letters* **121**, 090503 (2018).
- [15] M. Araújo, C. Branciard, F. Costa, A. Feix, C. Giarmatzi, and Č. Brukner, Witnessing causal nonseparability, *New Journal of Physics* **17**, 102001 (2015).
- [16] P. G. Kwiat, K. Mattle, H. Weinfurter, A. Zeilinger, A. V. Sergienko, and Y. Shih, New high-intensity source of polarization-entangled photon pairs, *Phys. Rev. Lett.* **75**, 4337–4341 (1995).
- [17] T. van der Lugt, J. Barrett, and G. Chiribella, Device-independent certification of indefinite causal order in the quantum switch, *Nature Communications* **14**, 5811 (2023).
- [18] Phuc Thai V., “Butterfly Image Classification Dataset,” Kaggle, 2022. Available at: <https://www.kaggle.com/datasets/phucthaiv02/butterfly-image-classification>
- [19] As in our phase-visibility estimators [Eqs. (11),(16)], the denominator is independent of the analyzer choice for C , canceling common-mode drifts and unequal efficiencies.